AIAA JOURNAL
Vol. 40, No. 9, September 2002

Time-Accurate Inlet and Outlet Conditions for Unsteady Transonic Channel Flow

J. Ballmann* and G. Britten†
Rheinisch-Westfälische Technische Hochschule Aachen, 52062 Aachen, Germany
and
I. Sofronov‡
Russian Academy of Sciences, 125047, Moscow, Russia

Nonlocal inlet and outlet transparent boundary conditions (TBCs) based on a linear model of the Euler equations outside the computational domain are studied. The conditions are tested for both stationary and nonstationary flow problems about an airfoil in the numerical wind tunnel. Comparison is made with characteristic-based boundary conditions (CBCFs). Test calculations show that TBCs require much smaller computational domains for solving the problem. Unsteady calculations for the oscillating airfoil show that the solutions obtained with TBCs and CBCFs can strongly differ from each other in the case of certain resonance frequencies. In contrast to CBCFs, TBCs permit us to observe much better coincidence of solutions while increasing the size of the computational domains used. It is also observed that calculations for resonance cases require greater computational domains (up- and downstream) and much more oscillating cycles to obtain a periodical solution.

I. Introduction

EXPERIMENTS in wind tunnels are and will remain an important basis for aerodynamical design. For stationary flow, the problem of wind-tunnel corrections, extrapolating wind-tunnel results to free flight conditions, is almost solved. However, for transonic flow, so-called adaptive walls[1,2] and ventilated walls[3] are still posing problems and require improvements of techniques. For unsteady and, particularly, for unsteady transonic flow, transmission of wind-tunnel test data to free flight conditions is still a challenging problem. Adaptive wall strategies for nonstationary flow are not well established yet. That has been the motivation for introducing a numerical wind tunnel with a measuring section of finite length that can also be applied to stationary adaptive walls and that enables us to simulate the experimental results in a wind tunnel correctly. This is a difficult task, yet necessary for the validation of a numerical method that will be applied later for free flight conditions. With the trend toward design improvement at lower costs, the accuracy and the reliability of numerical predictions are of increasing importance.

One of the crucial points for time-accurate predictions in wind tunnels are inlet and outlet boundary conditions. Some widely used characteristic-based boundary conditions, (for example, Refs. 4 and 5) may require rather large computational domains. However, even if inlet and outlet boundaries are placed far from the aerodynamic model to be investigated, such conditions can induce essential distortions to the solution (see examples in Sec. VI). Moreover, noting that for the time-accurate simulation, one has to use grids with spacings permitting the resolution of outgoing waves (to avoid spurious reflections), the size of computational domains can essentially influence computational costs.

To find more accurate artificial boundary conditions, we note that nonlinear and viscous effects can be neglected far from the measuring section. (A typical Reynolds number may reach some tens of millions for three-dimensional transonic aerodynamics.) Therefore, we use the time-dependent Euler equations, linearized about the constant uniform background of undisturbed flow at infinity, as a proper mathematical model in the far field. Our boundary conditions are exact with respect to this model, and, hence, they are nonlocal in both space and time. Note that different kinds of approximate boundary conditions based on the analysis of the linearized Euler equations have been derived, for example, by Gustafsson,[6] Giles,[7] and Kröner.[8] Simplifications proposed in the cited approaches aim to avoid the full nonlocalness in the conditions; otherwise, the computational efforts could be too expensive. The approach developed in this paper keeps the initial nonlocalness of boundary conditions (and, therefore their accuracy) and uses ideas from Refs. 9 and 10 to obtain computational formulas that are recurrent with respect to time. The mathematical framework and preliminary results for the problem under consideration may be found in Refs. 11 and 12, respectively. Note that similar boundary conditions are also discussed in Ref. 13.

The paper is organized as follows. The conditions are derived in Sec. II. In Sec. III, we describe a way to construct a discrete counterpart of them, yielding stable, recurrent with respect to time, and second-order-of-approximation difference formulas. A modification of the boundary conditions for finding stationary solutions is described in Sec. IV. Section V contains numerical aspects of the FLOWer code[14] used for the calculations. In Sec. VI, we present results obtained while modeling test flows in channels.

II. Mathematical Background of Transparent Boundary Conditions

A. Flow Model

Consider a problem of inviscid, nonheat-conducting perfect gas flow without body forces and body heat supply in an infinitely long channel having the constant height H outside a bounded computational domain. The undisturbed flow at $x \to -\infty$ is assumed to be homogeneous in space and time with constant specific entropy η everywhere. Downstream, the flow is generally not homogeneous because material pathlines may have crossed a shock where η undergoes a jump, depending on the local shock strength. However, farther downstream $D\eta/Dt = 0$ applies, so that the flow is isentropic but rotational and nonhomentropic, that is, $\eta \neq$ const everywhere.

We use Cartesian coordinates x and y with x directed along the channel. $V = (u, v)$, P ρ, and γ denote the velocity vector, pressure, density, and the ratio of specific heats, respectively. Linearization of the unsteady Euler equations in nonconservative form

Received 19 February 2001; revision received 5 January 2002; accepted for publication 22 January 2002.

*Professor, Faculty of Mathematics, Informatics and Science, Lehr- und Forschungsgebiet für Mechanik, Templergraben 64. Member AIAA.
†Ph.D. Student, Faculty of Mathematics, Informatics and Science, Lehr- und Forschungsgebiet für Mechanik, Templergraben 64.
‡Professor, Department of Applied Mathematics, Keldysh Institute of Applied Mathematics, Miusskaya Ploschad 4; sofronov@spp.keldysh.ru.

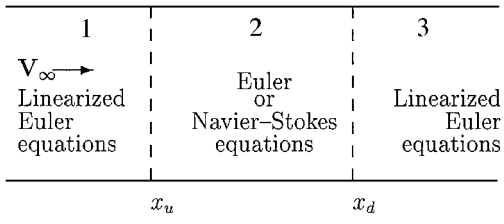

Fig. 1 Subdomains in the channel.

$$\boldsymbol{V}_t + (\boldsymbol{V}\,\mathrm{grad})\boldsymbol{V} + (1/\rho)\,\mathrm{grad}P = 0$$

$$P_t + \boldsymbol{V}\,\mathrm{grad}P + \gamma P\,\mathrm{div}\boldsymbol{V} = 0$$

$$\rho_t + \boldsymbol{V}\,\mathrm{grad}\rho + \rho\,\mathrm{div}\boldsymbol{V} = 0 \tag{1}$$

about the uniform, steady background at infinity u_∞, P_∞, and ρ_∞ results in the system

$$\tilde{\boldsymbol{V}}_t + u_\infty \tilde{\boldsymbol{V}}_x + (1/\rho_\infty)\,\mathrm{grad}\tilde{P} = 0$$

$$\tilde{P}_t + u_\infty \tilde{P}_x + \rho_\infty c_\infty^2\,\mathrm{div}\tilde{\boldsymbol{V}} = 0$$

$$\left(\tilde{P} - c_\infty^2\tilde{\rho}\right)_t + u_\infty\left(\tilde{P} - c_\infty^2\tilde{\rho}\right)_x = 0 \tag{2}$$

for perturbations $\tilde{\boldsymbol{V}} = \boldsymbol{V} - \boldsymbol{V}_\infty$, $\tilde{\rho} = \rho - \rho_\infty$, $\tilde{P} = P - P_\infty$, and $\boldsymbol{V}_\infty = (u_\infty, 0)$. Here $c_\infty^2 = \gamma P_\infty/\rho_\infty$ is the unperturbed sound speed squared.

Let $x = x_u$, $x = x_d$ be the coordinates for the upstream and downstream boundaries of the computational domain. We consider Eq. (2) as the flow model for $x < x_u$ and for $x > x_d$, that is, outside the computational domain $x_u \le x \le x_d$ (Fig. 1).

The subsonic freestream flow is considered:

$$0 \le u_\infty < c_\infty$$

Remark: Cases $u_\infty = c_\infty$ and $u_\infty > c_\infty$ require special treatments, which are not discussed here.

We will derive artificial boundary conditions on the boundaries at x_u and x_d from the explicit representation of general solutions of well-posed auxiliary initial boundary-value problems for Eqs. (2) in the subdomains 1 and 3.

B. Inflow Conditions

Let the functions $\tilde{\boldsymbol{V}}$, $\tilde{P}$, and $\tilde{\rho}$ satisfy Eq. (2) in domain 1, that is, at $x \le x_u$. We consider our problem with the following homogeneous boundary and initial conditions at $x = -\infty$ and time $t = 0$:

$$\tilde{\boldsymbol{V}}|_{x\to-\infty} \equiv 0, \qquad \tilde{P}|_{x\to-\infty} \equiv 0, \qquad \tilde{\rho}|_{x\to-\infty} \equiv 0, \qquad t \ge 0$$

$$\tilde{\boldsymbol{V}}|_{t=0} \equiv 0, \qquad \tilde{P}|_{t=0} \equiv 0, \qquad \tilde{\rho}|_{t=0} \equiv 0, \qquad x \le x_u \tag{3}$$

Our aim is to transfer conditions (3) from left-hand infinity to the inflow boundary $x = x_u$ of domain 2.

If we apply the rotation operator $\mathrm{rot}\,\tilde{\boldsymbol{V}} := \tilde{v}_x - \tilde{u}_y$ to the vector $\tilde{\boldsymbol{V}}$ in the first equation in Eq. (2) and conditions (3), we get the following problem:

$$(\mathrm{rot}\tilde{\boldsymbol{V}})_t + u_\infty(\mathrm{rot}\tilde{\boldsymbol{V}})_x = 0, \qquad \mathrm{rot}\tilde{\boldsymbol{V}}|_{x=-\infty} = 0$$

$$\mathrm{rot}\tilde{\boldsymbol{V}}|_{t=0} = 0 \tag{4}$$

Obviously, the solution to Eq. (4) in the domain $-\infty < x \le x_u$ satisfies

$$\mathrm{rot}\tilde{\boldsymbol{V}} = 0 \tag{5}$$

Therefore, the vector $\tilde{\boldsymbol{V}}$ is generated by a scalar potential $\Phi(t, x, y)$,

$$\tilde{\boldsymbol{V}} = \mathrm{grad}\Phi \tag{6}$$

Substituting Eq. (6) for $\tilde{\boldsymbol{V}}$ into the first equation in Eq. (2), we obtain

$$\mathrm{grad}\Phi_t + u_\infty\,\mathrm{grad}\Phi_x + (1/\rho_\infty)\mathrm{grad}\tilde{P} = 0$$

Hence,

$$\Phi_t + u_\infty\Phi_x + (1/\rho_\infty)\tilde{P} + f(t) = 0$$

where $f(t)$ is a function occurring due to integration. Because the fluid flow state is prescribed as constant at $-\infty$, we have $f(t) = 0$, and therefore,

$$\Phi_t + u_\infty\Phi_x + (1/\rho_\infty)\tilde{P} = 0 \tag{7}$$

If we replace $\tilde{\boldsymbol{V}}$ and $\tilde{P}$ by Eqs. (6) and (7) in the second equation in Eq. (2), we get the following equation for the potential Φ:

$$\Phi_{tt} + 2u_\infty\Phi_{tx} + u_\infty^2\Phi_{xx} - c_\infty^2\Delta\Phi = 0, \qquad -\infty < x < x_u \tag{8}$$

where Δ is the Laplacian.

Let us now write the boundary conditions for Φ. By an appropriate choice of an additive constant in the definition of Φ, a trivial condition at $x \to -\infty$ is obtained from Eqs. (3) and (6):

$$\Phi|_{x\to-\infty} = 0 \tag{9}$$

In addition, the the slip wall conditions $\tilde{v} = 0$ valid at the bottom and top walls of the channel (recall that we consider Euler flow) give us

$$\Phi_y|_{y=y_0} \equiv 0, \qquad \Phi_y|_{y=y_0+H} \equiv 0 \tag{10}$$

where y_0 is the coordinate of the bottom wall and H is the height of the channel.

The initial conditions at rest yield

$$\Phi|_{t=0} \equiv 0, \qquad \Phi_t|_{t=0} \equiv 0 \tag{11}$$

Our first step consists of finding a general solution to problem (8–11), which will then be used to derive the desired upstream boundary conditions. To represent this general solution in terms of a parametric function, we use a nonhomogeneous Dirichlet condition at $x = x_u$:

$$\Phi|_{x=x_u} = \Phi^0(t, y) \tag{12}$$

where the parametric function Φ^0 is defined from Eq. (7) supposing that $\tilde{P}$ and $\Phi_x \equiv \tilde{u}$ are given functions at $x = x_u$:

$$\Phi^0(t, y) \equiv -\int_0^t \left[\frac{1}{\rho_\infty}\tilde{P}(t', x_u, y) + u_\infty\tilde{u}(t', x_u, y)\right]\mathrm{d}t' \tag{13}$$

Thus, we have problem (8–12) for the potential Φ. It is solved by the method of separation of variables. We introduce the basis functions along the y direction,

$$\varphi_m(y) = \cos[m\pi(y - y_0)/H], \qquad y_0 \le y \le y_0 + H$$

$$m = 0, 1, 2, \ldots$$

and denote by Q the operator of summation with respect to φ_m in

$$\Phi(t, x, y) = \sum_{m=0}^{\infty}\Phi_m(t, x)\varphi_m(y) \tag{14}$$

and by Q^{-1} the inverse operator of calculating Fourier coefficients

$$\{a_m\}_{m=0}^{\infty} = Q^{-1}f$$

where

$$a_m := \frac{2}{H}\int_{y_0}^{y_0+H}\varphi_m(y)f(y)\,\mathrm{d}y, \qquad m > 0$$

$$a_0 := \frac{1}{H}\int_{y_0}^{y_0+H} f(y)\,\mathrm{d}y \tag{15}$$

[The use of cosines in Eq. (14) ensures the zero normal velocity at the walls of the channel; see Eq. (10).]

Exploring the Fourier and Laplace transforms technique, we find the solution of problem (8–12) in explicit form:

$$\Phi(t, x, y) = \Phi^0\left(t + \frac{x - x_u}{c_\infty - u_\infty}, y\right) + c_\infty(x - x_u)Q \times \int_0^{t + \frac{x - x_u}{c_\infty - u_\infty}} \{\bar{B}_m(t - t', x - x_u)\} Q^{-1}\Phi^0(t', y)\, dt' \qquad (16)$$

where $\{\}$ for B_m denote that each Fourier coefficient obtained by Q^{-1} is convolved with the corresponding kernel having the same subscript index m and where

$$\bar{B}_m(t, x) = (\lambda_m)^2 \frac{J_1[A_m(t, -x)]}{A_m(t, -x)}$$

$$\lambda_m = \frac{m\pi}{H}, \qquad \bar{B}_0(t, x) = 0$$

$J_1(x)$ is the Bessel function of first order, and

$$A_m(t, x) = \lambda_m \sqrt{c_\infty^2 - u_\infty^2} \times \sqrt{[t - x/(c_\infty - u_\infty)][t + x/(c_\infty + u_\infty)]}$$

Note that the nonlocal term, which appeared in Eq. (16), will result in nonlocal formulas for the desired boundary conditions.

From Eq. (3) and the third equation in Eq. (2), it follows that $\tilde{\rho} = \tilde{P}/c_\infty^2$, which corresponds to homentropic flow. Thus, formulas (13), (16), (6), and

$$\tilde{P} = -\rho_\infty u_\infty \Phi_x - \rho_\infty \Phi_t, \qquad \tilde{\rho} = \tilde{P}\big/c_\infty^2 \qquad (17)$$

supply the solution of system (2) in the domain $-\infty < x < x_u$ in terms of the function

$$(1/\rho_\infty)\tilde{P}(t, x_u, y) + u_\infty \tilde{u}(t, x_u, y)$$

given at $x = x_u$.

Now, let us take a solution $\tilde{V}$, $\tilde{P}$, and $\tilde{\rho}$ of Eq. (2) and obtain the relation between these functions at the cross section $x = x_u$. Dividing Eq. (16) by $x - x_u$ and passing to the limit as $x - x_u \to 0$, we have, at $x = x_u$,

$$-\Phi_t + (c_\infty - u_\infty)\Phi_x = (c_\infty - u_\infty)c_\infty Q \int_0^t \{B_m(t - t')\} Q^{-1}\Phi^0(t', y)\, dt' \qquad (18)$$

where the kernel of the convolution operator is given by

$$B_m(t) = \lambda_m \frac{J_1\left(\lambda_m t\sqrt{c_\infty^2 - u_\infty^2}\right)}{t\sqrt{c_\infty^2 - u_\infty^2}} \qquad (19)$$

For operators such as the one occurring on the right-hand side (RHS) of Eq. (18), we will use a simpler notation,

$$Q\{B_m\} * Q^{-1}\Phi^0$$

Substituting Eq. (7) for the left-hand side of Eq. (18), differentiating Eq. (18) with respect to time, and taking Eq. (13), we get the first desired relation:

$$\tilde{P}_t + \rho_\infty c_\infty \tilde{u}_t + c_\infty(c_\infty - u_\infty)Q\{B_m\} * Q^{-1}(\tilde{P} + \rho_\infty u_\infty \tilde{u}) = 0$$

at $x = x_u$.

The other two relations are obtained from Eqs. (5) and (17), and so the artificial boundary conditions at $x = x_u$ are

$$\tilde{P}_t + \rho_\infty c_\infty \tilde{u}_t + c_\infty(c_\infty - u_\infty)Q\{B_m\} * Q^{-1}(\tilde{P} + \rho_\infty u_\infty \tilde{u}) = 0$$
$$\tilde{v}_x - \tilde{u}_y = 0, \qquad \tilde{\rho} - \tilde{P}\big/c_\infty^2 = 0 \qquad (20)$$

C. Outflow Conditions

Let us consider now the functions $\tilde{V}$, $\tilde{P}$, and $\tilde{\rho}$ such that they satisfy Eqs. (2) at $x \geq x_d$, that is, in domain 3 (Fig. 1). Again we suppose that initial and boundary conditions are homogeneous:

$$\tilde{V}|_{x\to\infty} \equiv 0, \qquad \tilde{P}|_{x\to\infty} \equiv 0, \qquad \tilde{\rho}|_{x\to\infty} \equiv 0, \qquad t \geq 0$$
$$\tilde{V}|_{t=0} \equiv 0, \qquad \tilde{P}|_{t=0} \equiv 0, \qquad \tilde{\rho}|_{t=0} \equiv 0, \qquad x \geq x_d \qquad (21)$$

Now we will transfer conditions (21) from right-hand infinity to the outflow boundary $x = x_d$ of domain 3.

Obviously, we cannot follow the approach developed in the preceding section because the outflow can be both rotational and nonhomentropic. Therefore, we consider the downstream pressure, which is a natural function for practical flow problems. Differentiating the second equation in Eq. (2) with respect to t and x and applying the divergence operator to the first equation, we get

$$\tilde{P}_{tt} + u_\infty \tilde{P}_{tx} + \rho_\infty c_\infty^2 \operatorname{div}\tilde{V}_t = 0$$
$$\tilde{P}_{tx} + u_\infty \tilde{P}_{xx} + \rho_\infty c_\infty^2 \operatorname{div}\tilde{V}_x = 0$$
$$\operatorname{div}\tilde{V}_t + u_\infty \operatorname{div}\tilde{V}_x + (1/\rho_\infty)\Delta\tilde{P} = 0$$

Eliminating $\tilde{V}$, we obtain the following equation for the perturbation of pressure:

$$\tilde{P}_{tt} + 2u_\infty \tilde{P}_{tx} + u_\infty^2 \tilde{P}_{xx} - c_\infty^2 \Delta\tilde{P} = 0, \qquad x_d < x < \infty \qquad (22)$$

Evidently, the boundary and initial conditions for $\tilde{P}$ are

$$\tilde{P}|_{x\to\infty} = 0, \qquad \tilde{P}|_{t=0} = 0, \qquad \tilde{P}_t|_{t=0} = 0 \qquad (23)$$

Again, we will find a general solution to Eqs. (22) and (23) in terms of a parametric function P^0, which is the RHS of the Dirichlet condition

$$\tilde{P}|_{x=x_d} = P^0 \qquad (24)$$

If we substitute $-x$ for x and $-u_\infty$ for u_∞ in Eqs. (22–24), then the problem for the pressure becomes the same as the problem for Φ. Therefore, the solution of Eqs. (22–24) has the form

$$\tilde{P}(t, x, r, \varphi) = P^0\left(t - \frac{x - x_d}{c_\infty + u_\infty}, y\right) - c_\infty(x - x_d)Q \times \int_0^{t - \frac{x - x_d}{c_\infty + u_\infty}} \{\bar{B}_m(t - t', x - x_d)\} Q^{-1}P^0(t', y)\, dt' \qquad (25)$$

To obtain the desired condition for $\tilde{P}$ on the outflow boundary $x = x_d$, let us divide Eq. (25) by $x - x_d$ and take the limit as $x - x_d \to 0$. The result is

$$\tilde{P}_t + (c_\infty + u_\infty)\tilde{P}_x + c_\infty(c_\infty + u_\infty)Q \times \int_0^t \{\bar{B}_m(t - t', 0)\} Q^{-1}\tilde{P}(t', y)\, dt' = 0$$

or, in operator form,

$$\tilde{P}_t + (c_\infty + u_\infty)\tilde{P}_x + c_\infty(c_\infty + u_\infty)Q\{B_m\} * Q^{-1}\tilde{P} = 0 \qquad (26)$$

where the kernel B_m of the convolution operator is given by Eq. (19).

Combining Eqs. (2) and (26) to eliminate the derivative $\tilde{P}_x$, we get the desired boundary condition:

$$\tilde{P}_t - \rho_\infty c_\infty \tilde{u}_t + \rho_\infty c_\infty u_\infty \tilde{v}_y + \left(c_\infty^2 - u_\infty^2\right)Q\{B_m\} * Q^{-1}\tilde{P} = 0 \qquad (27)$$

D. Transparency of Boundary Conditions for the Linear Case

Equations (20) and (27) represent additional relations between the unknown functions on the boundary needed to close the governing equations inside the computational domain. To show that conditions (20) and (27) provide a well-posed linear problem and are exact, let us consider two problems, an initial boundary-value problem for the linearized Euler equations (2) in the whole channel $-\infty < x < \infty$, with homogeneous initial conditions at $t = 0$ for $x < x_u$ and $x > x_d$, and the problem for Eqs. (2) in the subdomain $x_u \le x \le x_d$, with the boundary conditions (20) and (27). We denote these problems as problem A and problem B, respectively. We are in the position to formulate the following statements; see details and proof in Ref. 11: 1) Let $\tilde{V}$, $\tilde{P}$, and $\tilde{\rho}$ be a solution of problem A; then $\tilde{V}$, $\tilde{P}$, and $\tilde{\rho}$ is the solution of problem B. 2) Conversely, let $\tilde{V}$, $\tilde{P}$, and $\tilde{\rho}$ be a continuously differentiable solution of problem B; then there exists the prolongation of $\tilde{V}$, $\tilde{P}$, and $\tilde{\rho}$ into the whole domain $-\infty < x < \infty$ to the solution of problem A. Note that this prolongation has the explicit form based on formulas (16) and (25).

As for the well posedness of the original nonlinear problem in the computational domain with the proposed boundary conditions, this question is, evidently, equivalent to the well posedness of the coupled linear–nonlinear problem in the channel of infinite length (Fig. 1). We do not discuss this question here.

III. Numerical Implementation of Transparent Boundary Conditions

Incorporation of our boundary conditions into a step-by-step integration scheme of the governing equations in the computational domain is made as follows. We suppose that the solution is known at the nth time level t^n on the entire computational grid, including the boundary points and on the $(n+1)$th time level t^{n+1} at internal grid points. Then the boundary conditions are used to update the solution at t^{n+1} at the boundary points.

We assume that near to the inflow and outflow boundaries, the grid has a simple structure such that two layers of neighboring grid points (named external and internal) lie on the corresponding neighboring cross sections. Denote the coordinates of these layers by x_e and x_i, respectively.

A. Inflow Section

It is more convenient to use directly the potential Φ to evaluate the required functions $X \equiv (\tilde{\rho}, \tilde{u}, \tilde{v}, \tilde{P})$ at boundary points instead of conditions (20), which is, of course, equivalent from the mathematical point of view. We introduce the following stencil in (x, t) coordinates [with the y axis perpendicular to the (x, t) plane] to treat Eqs. (6), (7), and (18) (Fig. 2); here, $x_e = x_u$ of Fig. 1.

In Fig. 2, the four dots denote the grid points (along the y direction) with the coordinates x_e and x_i on the time levels t^n and t^{n+1}, respectively. The squares denote auxiliary points to calculate the potential. In accord with the preceding assumption, we know the values of X_i^n, X_e^n, X_i^{n+1}, Φ_i^n, and Φ_a^n. Our aim is to evaluate X_e^{n+1} and Φ_a^{n+1}. Denote the grid and time steps by $h = |x_i - x_e|$ and $\tau = t^{n+1} - t^n$, respectively. First, we estimate Φ_i^{n+2} by using central differences for approximating (7):

$$\Phi_i^{n+2} := \Phi_i^n - 2\tau\left[u_\infty \tilde{u}_i^{n+1} + (1/\rho_\infty)\tilde{P}_i^{n+1}\right] \tag{28}$$

Then we approximate Eq. (18) by the central difference scheme at the point (x_e, t^{n+1}):

$$-\frac{\Phi_a^{n+2} + \Phi_i^{n+2} - \Phi_a^n - \Phi_i^n}{2\tau} + (c_\infty - u_\infty)\frac{\Phi_i^{n+2} + \Phi_i^n - \Phi_a^{n+2} - \Phi_a^n}{2h} = (c_\infty - u_\infty)c_\infty S\left(\Phi_e^{n-1}, \Phi_e^n, \Phi_e^{n+1}\right) \tag{29}$$

where S is an approximation of the operator $Q\{B_m\} * Q^{-1}$ that we will consider in detail in Sec. III.C. Functions entering the RHS of Eq. (29) are defined as follows:

$$\Phi_e^{n-1} = \left(\Phi_a^{n-1} + \Phi_i^{n-1}\right)/2$$

known from the previous time level, and

$$\Phi_e^n = \left(\Phi_a^n + \Phi_i^n\right)/2, \qquad \Phi_e^{n+1} = \left(\Phi_a^n + \Phi_i^{n+2}\right)/2$$

Substituting (28) into (29) permits us to find Φ_a^{n+2} and then to use central differences for approximating Eqs. (6) and (17) to calculate X at the point (x_e, t^{n+1}).

B. Outflow Section

We have only one boundary condition (27) at $x = x_d$. To define all four components of X, we need three further equations. They are obtained from Eq. (2) and have the form

$$\tilde{v}_t + u_\infty \tilde{v}_x + (1/\rho_\infty)\tilde{P}_y = 0 \tag{30}$$

$$\left(\tilde{P} - c_\infty^2 \tilde{\rho}\right)_t + u_\infty \left(\tilde{P} - c_\infty^2 \tilde{\rho}\right)_x = 0 \tag{31}$$

$$(\tilde{P} + \rho_\infty c_\infty \tilde{u})_t + (u_\infty + c_\infty)(\tilde{P} + \rho_\infty c_\infty \tilde{u})_x + \rho_\infty c_\infty^2 \tilde{v}_y = 0 \tag{32}$$

Equation (32) is a linear combination of the equation for $\tilde{u}$ entering the first equation in Eq. (2) and the second equation in Eq. (2). As practical computations have shown, it provides a more stable algorithm compared with using just the equation for $\tilde{u}$.

Discretization of Eqs. (27) and (30–32) is executed similarly to the inflow conditions but with a simpler stencil (Fig. 3); here x_e corresponds with x_d in Fig. 1.

We approximate Eqs. (27) and (30–32) by using central differences at the central point $[(x_i + x_e)/2, (t^n + t^{n+1})/2]$. This includes the evaluation of the nonlocal term in Eq. (27) by its representation as

$$\left(c_\infty^2 - u_\infty^2\right) S\left(\tilde{P}_c^{n-0.5}, \tilde{P}_c^n, \tilde{P}_c^{n+0.5}\right) \tag{33}$$

where $\tilde{P}_c^{n-0.5}$ is known from the previous time level, $\tilde{P}_c^n = (\tilde{P}_e^n + \tilde{P}_i^n)/2$, and

$$\tilde{P}_c^{n+0.5} = \left(\tilde{P}_i^n + \tilde{P}_i^{n+1} + \tilde{P}_e^n + \tilde{P}_e^{n+1}\right)/4 \tag{34}$$

(See Sec. III.C.)

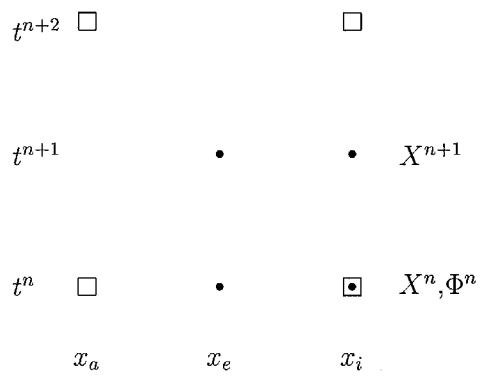

Fig. 2 Stencil for inflow conditions in (x, t) coordinates.

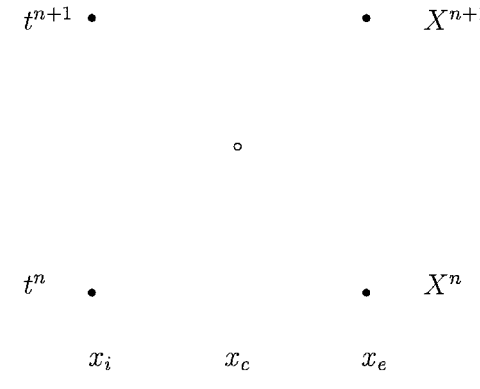

Fig. 3 Stencil for outflow conditions in (x, t) coordinates.

The derivatives with respect to y in the central point are evaluated by using mean values in accordance to Eq. (34).

Such an approximation of Eqs. (27) and (30–32) is implicit for the point (x_e, t^{n+1}) Therefore, we use simple iterations starting from an initial guess $X_e^{n+1} := X_i^{n+1}$ for evaluating derivatives with respect to y and the nonlocal term in Eq. (33). One or two iterations are usually required.

C. Evaluation of Operator S

The operator $Q\{B_m\} * Q^{-1}$ is nonlocal in both space and time. As to the space nonlocalness, a reasonable way of treating Fourier series is the use of corresponding finite Fourier sums. Therefore, we explore discrete counterparts to Eqs. (14) and (15) while evaluating S. A more difficult question is the nonlocalness with respect to time. A direct discretization of the convolution integral by an appropriate quadrature formula could result in a very expensive algorithm in the case of long time simulations with several thousand time levels.

The convolution kernel (19) is expressed in terms of the function $J_1(t)/t$. To localize the calculations in time, we represent $J_1(t)/t$ by a finite sum of exponentials:

$$B(t) = \frac{J_1(t)}{t} \approx \sum_{l=1}^{L} b_l e^{\beta_l t} \tag{35}$$

This is made numerically by approximating the Laplace transform of $J_1(t)/t$, that is, the function $\sqrt{(s^2+1)} - s$, in terms of rational functions. (We use the known fact that the inverse Laplace transform of a rational function with simple poles is a sum of exponentials.) For instance, one of the possible sets of numbers $\{b_l, \beta_l\}$, $l = 1, \ldots, 16$, that we have found in Eq. (35) (using corresponding procedures from the MAPLE package) does provide the accuracy 10^{-5} for $0 \le t < \infty$; that can be considered sufficient for most practical applications.

According to Eqs. (18) and (27), we have to evaluate the convolution integral

$$g(t) = \int_0^t B(t-t')\, f(t')\, \mathrm{d}t'$$

for a function $f(t)$. Using Eq. (35), we obtain

$$g(t) \approx \sum_{l=1}^{L} b_l \int_0^t e^{\beta_l (t-t')} f(t')\, \mathrm{d}t' = \sum_{l=1}^{L} b_l A_l(t) \tag{36}$$

where

$$A_l(t) := \int_0^t e^{\beta_l (t-t')} f(t')\, \mathrm{d}t'$$

Let τ be a time step. Then the functions A_l can be represented as follows:

$$A_l(t) = e^{\beta_l \tau} A_l(t-\tau) + \int_{t-\tau}^{t} e^{\beta_l (t-t')} f(t')\, \mathrm{d}t' \tag{37}$$

We see from Eq. (36) that the convolution integral $g(t)$ is evaluated by the sum of functions $A_l(t)$, each of them calculated by the recurrence formula (37). This means that nonlocal-in-time formulas (18) and (27) are approximated by local-in-time calculation formulas [with any desired accuracy depending on accuracy of the representation (35)].

The integral in Eq. (37) is evaluated numerically by Simpson's rule. In our case, the three points required for this rule are (t^{n-1}, t^n, t^{n+1}) and $(t^{n-0.5}, t^n, t^{n+0.5})$ for Eqs. (29) and (33), respectively.

D. Approximation Accuracy and Stability

We have three sources of approximation error while discretizing our boundary conditions: approximation of 1) functions and derivatives, 2) integrals in Eq. (37), and 3) kernel of the convolution integral [see Eq. (35)]. Central differences and central averages used for derivatives and functions, respectively, to discretize local terms in Eqs. (6), (7), (17), (18), (27), and (30–32) provide second order of approximation with respect to space and time.

Simpson's rule permits us to keep this order of accuracy while handling Eq. (37). As to the source 3, it has another nature, not connected with the grid. All calculations for the examples in Sec. VI have been done with a concrete set of $\{b_l, \beta_l\}$ [see Eq. (35)] having the mentioned accuracy 10^{-5}. Additional calculations for several same examples with another, less accurate, set have shown that this change does not have a significant influence on the solutions. However, for much finer grids, one must perhaps find sets of $\{b_l, \beta_l\}$ with better approximation properties.

The question of stability is more delicate. One must consider it for the coupled discrete system of nonlinear equations in the computational domain and on the boundary. However, this is beyond the scope of the current study. We observed in computations that both the difference scheme inside the computational domain and the discrete formulas on the boundaries can produce instability, but fortunately with much higher values of the time step than those prescribed from the criterion of required accuracy.

IV. Finding Steady-State Solutions

Unsteady simulation, such as the oscillation of an airfoil, is started from a stationary solution. The steady-state solution is usually obtained by a transient process for the original time-dependent equations, where time t does not have a physical meaning actually. Therefore, we must exclude the physical time from the formulas of the proposed boundary conditions, considering for this purpose the asymptotically steady case as $t \to \infty$. Evidently this will give us a certain kind of exact boundary conditions in the steady linearized case, which are adapted also to a transient procedure.

Because the final solution does not depend on the time step τ, we do not change our formulas as for time derivatives. [However, the rate of convergence can depend on τ, which now plays the role of an iterative parameter; therefore, an appropriate magnitude of τ can be chosen to obtain an optimal convergence rate (see Sec. VI).] We have to make only some changes in treating the operator S because it keeps the history of the convergence. Let us consider a limit case of Eq. (37) as $t \to \infty$. We have $f(t) \to \text{const} =: f_l$, $A_l(t) \to A_l (= \text{const})$ and, therefore,

$$A_l = e^{\beta_l \tau} A_l + f_l \int_{t-\tau}^{t} e^{\beta_l (t-t')}\, \mathrm{d}t' = e^{\beta_l \tau} A_l - \frac{f_l}{\beta_l}(1 - e^{\beta_l \tau})$$

Hence,

$$A_l = -f_l/\beta_l \tag{38}$$

Thus we use Eq. (38) while evaluating S during iterations for finding steady-state solutions.

Note that a direct analysis of the steady linearized Euler equations model has been performed in Ref. 15 to obtain accurate boundary conditions.

V. Implementation Aspects of Nonstationary Flow Calculations on a Moving Grid

For the fluid flow calculations, the FLOWer code is employed, which is being used and further developed in the project MEGAFLOW by different German research organizations, among them Lehr- und Forschungsgebiet für Mechanik at Rheinisch-Westfalische Technische Hochschule Aachen. The project leadership is at DLR, German Aerospace Research Center/Brunswick.[16]

The FLOWer code solves optionally the Euler or the Reynolds averaged Navier–Stokes equations for three-dimensional compressible fluid flow. For unsteady flow about bodies in arbitrary motion a formulation with time-dependent finite volume has been introduced in Ref. 14. For purposes of computational aeroelasticity, a deforming grid algorithm has been implemented.[17]

The equations solved in this paper read (two-dimensional, strong conservation form of the Euler equations)

$$\frac{\partial}{\partial t} \int_{V(t)} \boldsymbol{U}\, \mathrm{d}V + \int_{\partial V(t)} \bar{F} \boldsymbol{n}\, \mathrm{d}S = 0$$

where $\boldsymbol{U} = (\rho, \rho u, \rho v, \rho e)^T$ is the vector of the conserved quantities: density, Cartesian components of momentum, and total specific

Table 1 Lift and drag coefficients for TBCs and CBCFs depending on the computational domain length

	$M_\infty = 0.5$				$M_\infty = 0.73$			
	TBCs		CBCFs		TBCs		CBCFs	
Size	C_l	C_d	C_l	C_d	C_l	C_d	C_l	C_d
S	0.2657	0.001397	0.2609	0.001559	0.3979	0.001444	0.3941	0.001547
M	0.2659	0.001392	0.2659	0.001395	0.3981	0.001443	0.3984	0.001446
L	0.2659	0.001392	0.2660	0.001393	0.3980	0.001442	0.3972	0.001465

energy density. In a moving grid with the grid velocity field $\tilde{V}_B$, the flux density matrix $\bar{F}$ is represented by

$$\bar{F} = \begin{bmatrix} \rho(V - V_B) \\ \rho u(V - V_B) + p i_x \\ \rho v(V - V_B) + p i_y \\ \rho e(V - V_B) + pV \end{bmatrix}$$

and n is the unit outer normal vector on the surface.

When started with an elliptically smoothed grid for the nondeformed reference configuration, the grid is adapted algebraically to the current configuration. Thereby, interpolation polynomials are used such that the nodes on the airfoil's surface are taken as material points throughout the motion, whereas the nodes at the outer boundary, which is the boundary of the computational domain, remain fixed in a rigid-body fixed coordinate system. Thus, the grid is deforming with time, and the nodes of the finite volumes within the flow field are moved such that a body surface fitting grid is ensured.

For the discretization in space, a second-order-accurate central cell-vertex finite volume formulation on block-structured grids is used.[16] Its earlier form is according to Ref. 18. Dual stepping[19] is implemented for time integration.

Within each time step, an explicit five-stage Runge–Kutta method is used providing second-order accuracy in time and a large stability range. It is accelerated by techniques of local pseudotime stepping, enthalpy damping, and implicit residual smoothing. The solution procedure is embedded into a sophisticated multigrid algorithm.

VI. Numerical Results

We study the performance of the introduced boundary conditions by conducting calculations for each test setup twice: imposing commonly used characteristic-based boundary conditions (CBCFs) and imposing transparent boundary conditions (20) and (27) (TBCs), respectively. (All other test parameters remain the same.) Because of the absence of reference solutions for the considered nonlinear Euler flows, we performed calculations with different lengths of the channel at fixed flight conditions. Evidently, for ideal boundary conditions, the solution must not depend on the size of the computational domain. Therefore, we believe that the tested boundary conditions are sufficiently accurate if they provide closer and closer solutions while increasing the lengths of the upstream and downstream regions of the computational domain (having a sufficiently fine grid to resolve generated waves).

A. Calculation of Steady-State Solutions for the Airfoil in Channel

A stationary flow about the British Aircraft Corp. airfoil[20,21] BAC 3-11/RES/30/21 has been calculated by using the FLOWer code for three different sizes of the channel: large (L), medium (M), and small (S) (Fig. 4). Two types of boundary conditions are compared: TBCs and a certain kind of CBCF according to Ref. 18, which refers to Ref. 22. The numbers of grid cells are 6912, 6144, and 4864 for the considered domains, whereby the grids for the smaller domains are subgrids of the large grid with the same spacing. Table 1 contains the lift and drag coefficients (C_l and C_d) for the regimes with Mach number $M_\infty = 0.5$ and 0.73. We see that TBCs provide better approximations of the aerodynamic coefficients (closer values to each other) calculated on the three considered computational domains compared with the CBCFs.

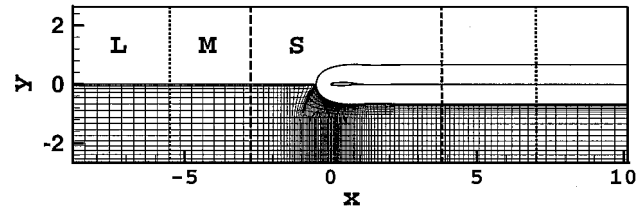

Fig. 4 Geometry of three computational domains: dotted and dashed lines denote the boundaries of the medium and small computational domains, respectively. Mesh in one of the blocks is shown. (Thin lines are the internal boundaries of grid blocks.)

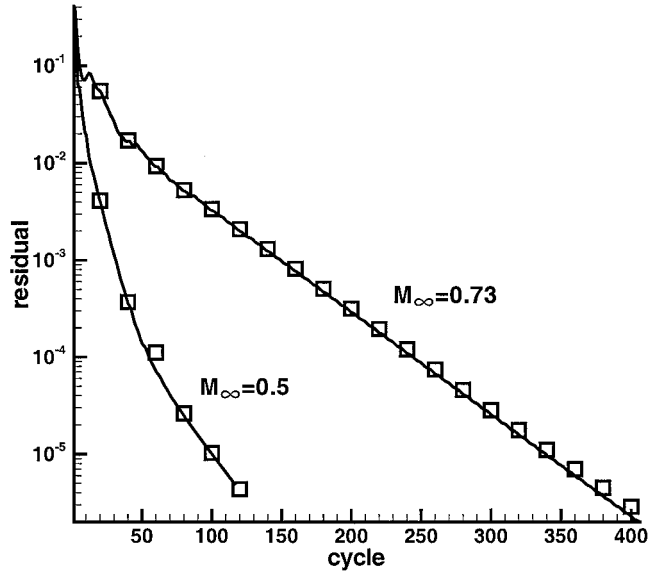

Fig. 5 Convergence history for the large domain with CBCFs (——) and TBCs (symbols).

Figure 5 shows the convergence history (residual vs number of multigrid cycles) for the calculations in the L domain. We see that the rate of convergence is nearly the same for both types of conditions. (Similar situations are observed for M and S domains.) Note that the additional computational costs required by TBCs are within 3% of the total CPU time.

B. Unsteady Computations

The unsteady computations have been performed for the oscillating airfoil by using stationary results as the starting solution. The comparative study was made for CBCFs and TBCs in L, M, and S computational domains.

According to Ref. 3, which refers to Ref. 23, there exists a set of resonance frequencies between an oscillating airfoil and the wind-tunnel walls:

$$\omega_m = (\pi/H)(2m - 1)c_\infty \sqrt{1 - M_\infty^2}, \qquad m = 1, 2, \ldots \tag{39}$$

where H is the height of the channel.

When we look at the nonlocal-in-time term in TBCs (18) and (27), we see that its main contribution to the equation is expected near the first frequency $\omega_1 \equiv \lambda_1 \sqrt{(c_\infty^2 - u_\infty^2)}$ [see Eq. (19)] because of the asymptotic behavior of the kernel function[24]:

$$\frac{J_1(\omega_1 t)}{\omega_1 t} \approx -\sqrt{\frac{2}{\pi}}\frac{\cos[\omega_1(t+\pi/4)]}{(\omega_1 t)^{\frac{3}{2}}}, \qquad t \to \infty$$

Indeed, the amplitude of the convolution integral for the periodical function $\cos(\omega_1 t)$ will grow with respect to time due to the contribution of the positive term

$$\frac{\cos^2(\omega_1 t)}{(\omega_1 t)^{\frac{3}{2}}}$$

By introducing the reduced frequencies $k = \omega l/(2u_\infty)$, where l is the chord length of the airfoil, we can rewrite Eq. (39) in the following form:

$$k_m = (\omega_m/2)(l/u_\infty) = (\pi/2)(l/H)\left(\sqrt{1-M_\infty^2}\Big/M_\infty\right)(2m-1) \tag{40}$$

Periodical solutions in a wind tunnel may contain frequencies near resonances (39). Practical calculations show (for example, see Ref. 2) that 1) solutions for resonance cases differ strongly from corresponding free flight solutions and 2) the interval of frequencies, where the difference is essential, is large enough. The interval of frequencies is measured in terms of the ratio l/H in Ref. 2; see our Eqs. (40).

That is why we concentrated our study of oscillating solutions first for resonance cases.

The lowest of the resonance frequencies (40) has the value $k_1 \approx 0.5133$ for $M_\infty = 0.5$ and $k_1 \approx 0.2775$ for $M_\infty = 0.73$, when it is taken into account that $l/H = 1/5.3$ for the geometry used.

We prescribe the oscillations of the angle of attack (degrees) of the airfoil by

$$\alpha(t) = \alpha_0 \sin \omega t, \qquad \alpha_0 = -3$$

with the fixed point at $l/4$ downstream of the leading edge. Figures 6 and 7 show the time history of the calculations for $M_\infty = 0.73$ and $k = 0.28$ using CBCFs and TBCs, respectively. (The time is measured in seconds if the geometry sizes are in meters in Fig. 4.) The details for two cycles of these calculations are shown in Figs. 8 and 9. We see that the CBCFs give quite different solutions depending on the size of the computational domains. However, the TBCs provide almost the same solutions for the M and L domains (solid and dotted lines practically merge in Fig. 9); the solution of the S domain (dashed line in the Fig. 9) is also sufficiently close to the other solutions.

The calculations with TBCs were continued up to the time $t = 2.5$ to be sure that our nonlocal-in-time conditions are stable.

Because of the observed convergence to a limit curve as the size of the computational domain increases (Fig. 9), we may conclude that the solution obtained with TBCs for the large domain is a true solution to the considered problem in the numerical wind tunnel.

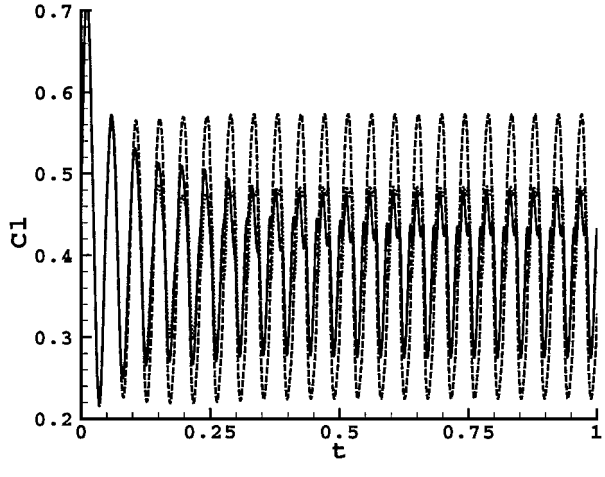

Fig. 6 C_l **vs** t **for L (——), M (· · · ·), and S (– – –) domains;** $M_\infty = 0.73$, $k = 0.28$, **CBCFs.**

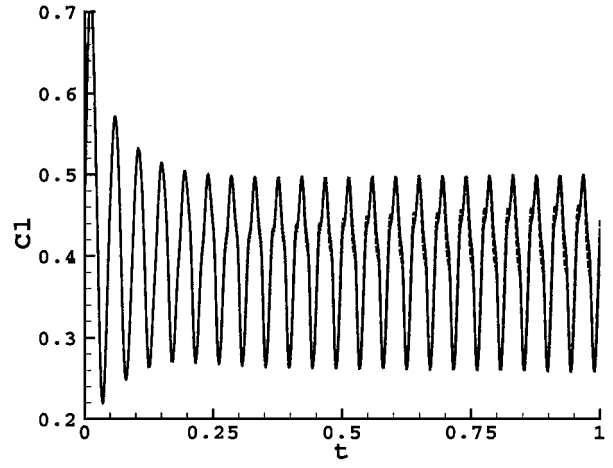

Fig. 7 C_l **vs** t **for the L (——), M (· · · ·), and S (– – –) domains;** $M_\infty = 0.73$, $k = 0.28$, **TBCs**

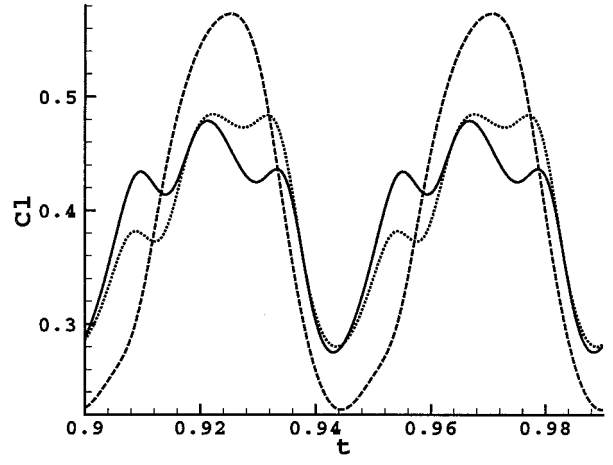

Fig. 8 Details of oscillating cycle from Fig. 6.

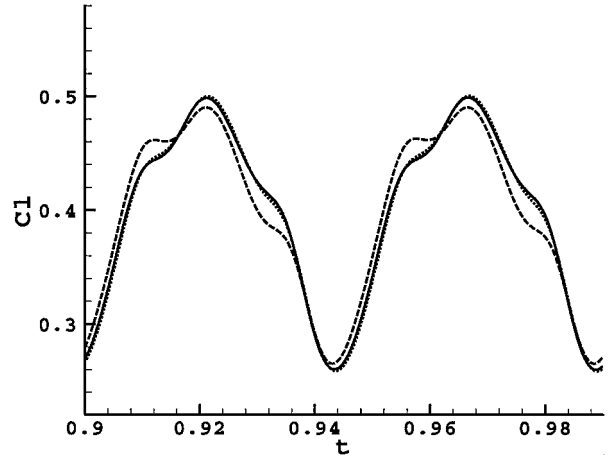

Fig. 9 Details of oscillating cycle from Fig. 7.

Figure 10 shows the limit-oscillation cycles, that is, periodical solutions observed after calculation of a large number of cycles, of the lift coefficient C_l vs angle of attack α for the solutions calculated within the L domain with TBCs and CBCFs, respectively. We see a remarkable difference between them. If we consider a nonresonance case with $k = 0.40$, the difference of solutions with TBCs and CBCFs is not as big (Fig. 11). An even smaller difference is observed for the case $k = 0.20$. For the latter, we show, in Fig. 12, the solution obtained with TBCs for the L domain. Figure 13 shows the difference values between this solution and solutions with TBCs for the S

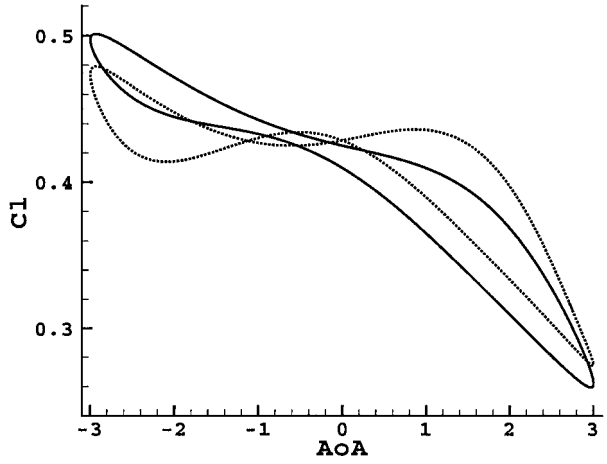

Fig. 10 C_l vs α for L domain with TBCs (——) and CBCFs (· · · ·); $M_\infty = 0.73, k = 0.28$ (resonance case).

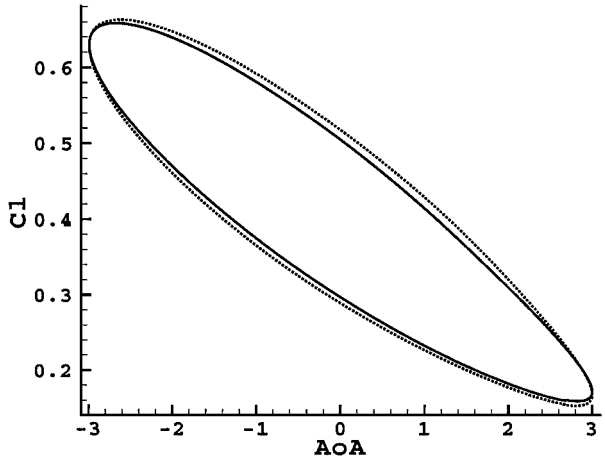

Fig. 11 C_l vs α for L domain with TBCs (——) and CBCFs (· · · ·); $M_\infty = 0.73, k = 0.40$ (nonresonance case).

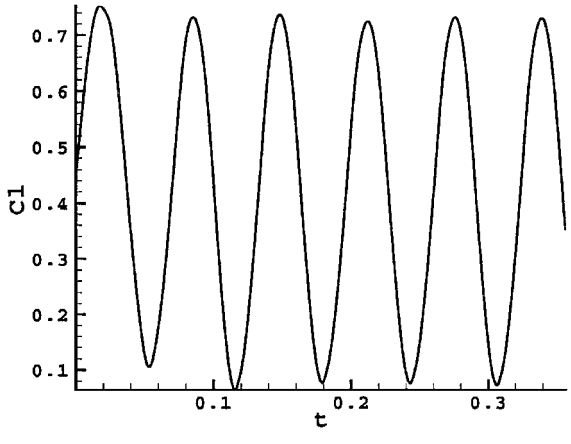

Fig. 12 C_l vs t for L domain; $M_\infty = 0.73, k = 0.20$, TBCs.

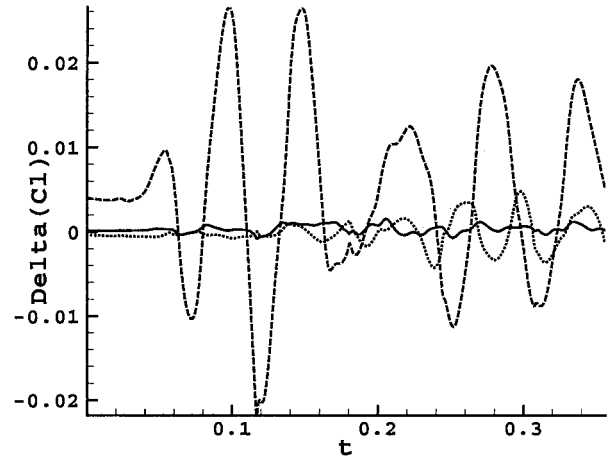

Fig. 13 Difference between solution shown in Fig. 12 and solutions with TBCs in S domain (——), with CBCFs in L domain (· · · ·), and with CBCFs in S domain (- - -); $M_\infty = 0.73, k = 0.20$.

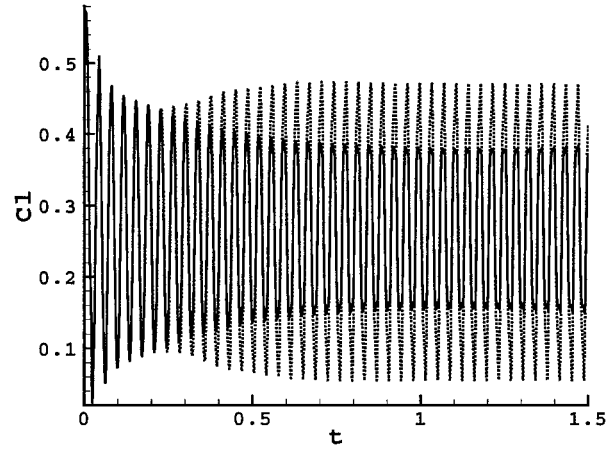

Fig. 14 C_l vs t for L domain with TBCs (——) and CBCFs (· · · ·); $M_\infty = 0.5, k = 0.51$.

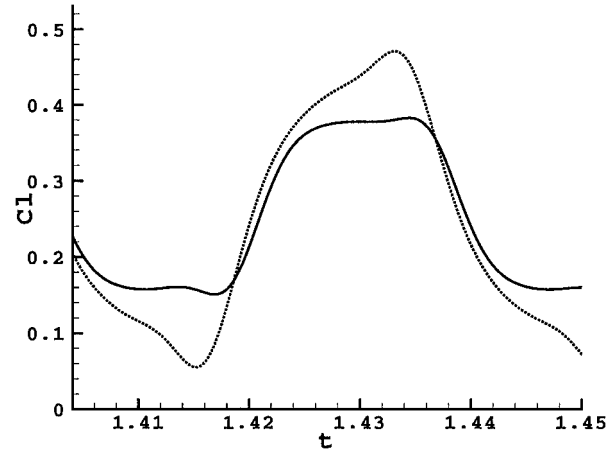

Fig. 15 Closeup of Fig. 14.

domain (solid line), with CBCFs for the L domain (dotted line), and with CBCFs for the S domain (dashed line), respectively. Because both solutions with TBCs are very close to each other, we consider the solution from Fig. 12 as the reference one. We see that solutions with CBCFs deviate much more from the reference solution, even for the L domain. An important issue of these results is that we can use S computational domains with TBCs for nonresonance cases.

The next set of calculations has been made for the subsonic case with $M_\infty = 0.5$. Figure 14 shows the time history for the calculations in the L domain with TBCs and CBCFs; the details for a little more than one oscillating cycle are shown in Fig. 15. We observe a big difference between the two solutions. Results for different sizes of the computational domain are presented in Fig. 16 (CBCFs) and Fig. 17 (TBCs). Even for TBCs, it is precarious to say that we have a convergence to a true solution. However, the only reason for such caution is that the linear model used while constructing TBCs might not be sufficiently accurate for the considered parameters of the test case. Therefore, we have repeated our calculations with half of the

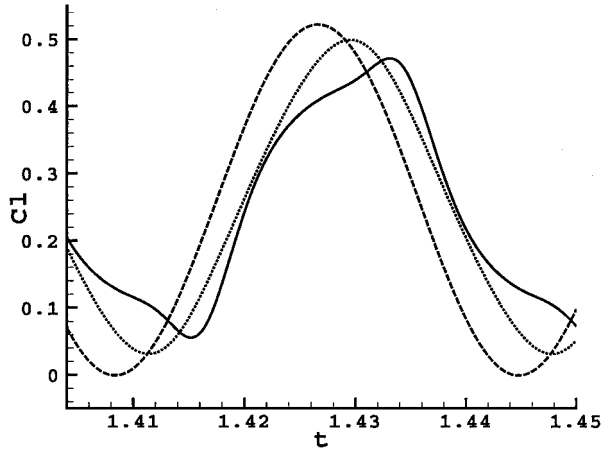

Fig. 16 C_l vs t for L (——), M (· · · ·), and S (– – –) domains; $M_\infty = 0.5$, $k = 0.51$, CBCFs, $\alpha_0 = 3$ deg.

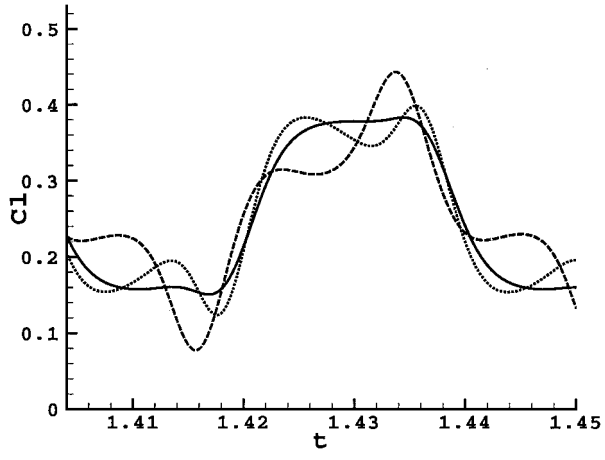

Fig. 17 C_l vs t for the L (——), M (· · · ·), and S (– – –) domains; $M_\infty = 0.5$, $k = 0.51$, TBCs, $\alpha_0 = 3$ deg.

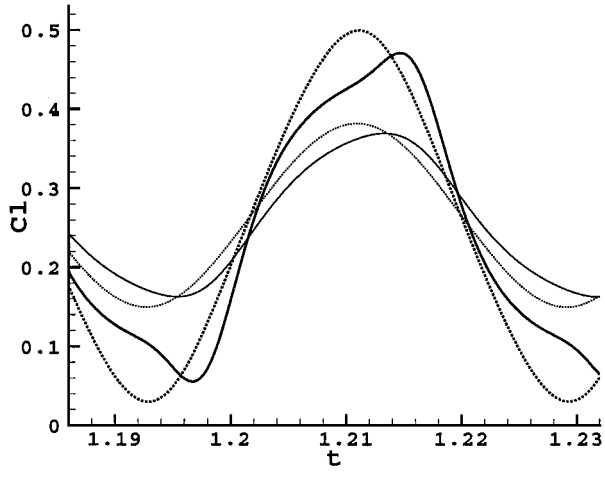

Fig. 18 C_l vs t for L (——) and M (· · · ·) domains; $M_\infty = 0.5$, $k = 0.51$, CBCFs, $\alpha_0 = 3$ deg (——), and $\alpha_0 = 1.5$ deg (····).

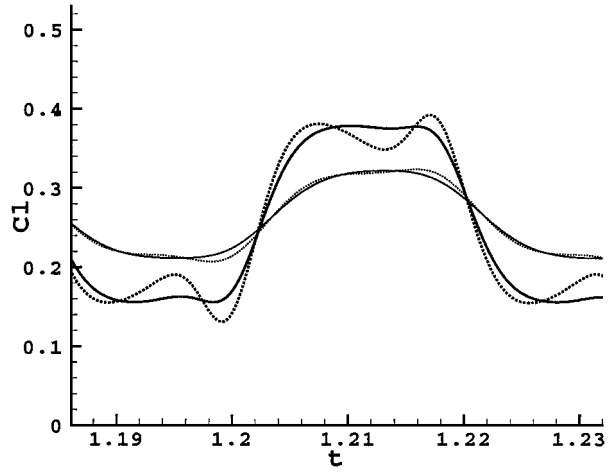

Fig. 19 C_l vs t for L (——) and M (· · · ·) domains; $M_\infty = 0.5$, $k = 0.51$, TBCs, $\alpha_0 = 3$ deg (——), and $\alpha_0 = 1.5$ deg (····).

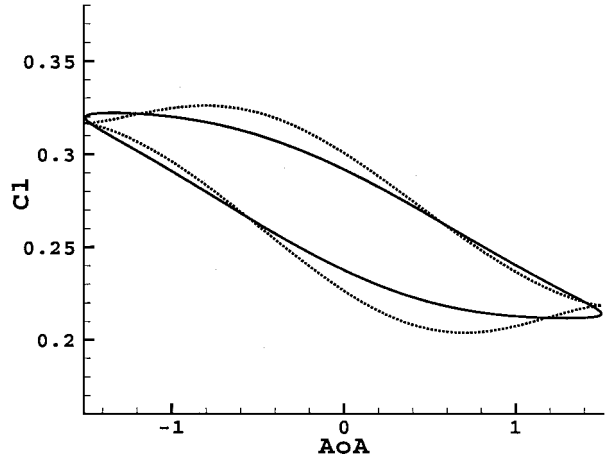

Fig. 20 C_l vs α for L (——) and M (· · · ·) domains; $M_\infty = 0.5$, $k = 0.51$, $\alpha_0 = 1.5$ deg, TBCs.

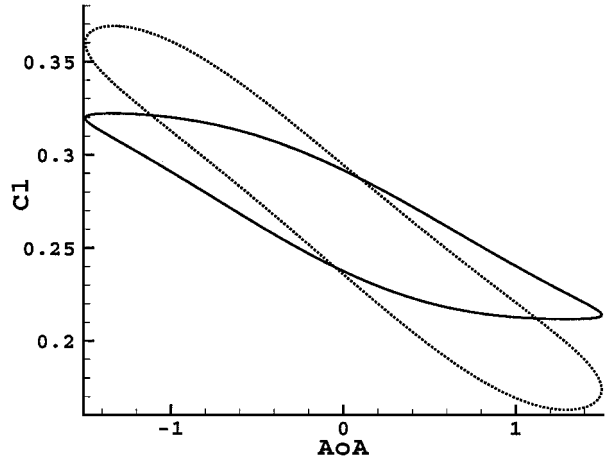

Fig. 21 C_l vs α for L domain with TBCs (——) and CBCFs (· · · ·); $M_\infty = 0.5$, $k = 0.51$, $\alpha_0 = 1.5$ deg.

value for the amplitude of the angle of attack ($\alpha_0 = 1.5$ deg), which should reduce the error of linearization. The results are shown in Fig. 18 (CBCFs) and Fig. 19 (TBCs) in comparison with the results for the 3-deg amplitude. Indeed, we can see that solutions with TBCs for the M and L domains are much closer to each other for the smaller amplitude. Figure 20 shows the limit oscillating cycles for these two solutions. The corresponding comparison of solutions with TBCs and CBCFs for the L domain is given in Fig. 21.

VII. Conclusions

Nonlocal inlet and outlet conditions have been implemented into the FLOWer code for unsteady compressible fluid flow calculations in channels. These conditions are time accurate with respect to the Euler equations linearized about the uniform constant mean flow outside the computational domain. They are based on the analysis of the wave equation in the moving fluid for the potential of the velocity in the upstream region and for the pressure in the downstream region, respectively.

The conditions are also adapted to predict steady-state solutions, and they permit us to explore accelerating techniques within FLOWer. The numerical implementation of the conditions has second-order accuracy of approximation in space and time.

The method permits a straightforward extension to three dimensions because it is based on the Fourier expansion of unknown functions on the boundary in terms of eigenfunctions of the Laplace operator considered in the wind tunnel cross section, operators Q and Q^{-1} in Eqs. (20) and (27); the main analysis concentrates on the corresponding one-dimensional harmonics (cf. Ref. 11).

Test calculations show that TBCs require much smaller sizes of the computational domain for obtaining both stationary and nonstationary solutions, compared with calculations using the standard CBCFs.

Unsteady calculations for the oscillating airfoil show that the solutions obtained with TBCs and CBCFs can strongly differ from each other in the case of the resonance reduced frequencies.[3,22] In contrast to CBCFs, TBCs permit us to observe the convergence to a true solution while increasing the size of the computational domain. The reason lies in the more accurate physical model used while constructing TBCs. Note that calculations for resonance cases require greater sizes of the computational domain (up- and downstream) and much more oscillating cycles to obtain a periodical solution.

Acknowledgments

This work has been supported by the Deutsche Forschungsgemeinschaft in the Collaborative Research Centre SFB (Sonderforschungsbereich) 401 "Modulation of Flow and Fluid-Structure Interaction at Airplane Wings" of the Rheinisch-Westfalische Technische Hochschule Aachen University of Technology. The third author was also partially supported by Russian Foundation of Basic Research Project 01-01-00520.

References

[1]Foersching, H., and Voss, R., "Adaptation for Unsteady Flow," *Adaptive Wind Tunnel Walls: Technology and Applications*, AR-269, AGARD, April 1990, pp. 91–99.

[2]Chang, B.-H., and Sung, B., "Usteady Adaptive Wall Models for Wind-Tunnel Testing," *AIAA Journal*, Vol. 33, No. 8, 1995, pp. 1536–1538.

[3]Fromme, J. A., and Golberg, M. A., "Aerodynamic Interference Effects on Oscillating Airfoils with Controls in Ventilated Wind Tunnels," *AIAA Journal*, Vol. 18, No. 4, 1980, pp. 417–426.

[4]Hirsch, C., *Numerical Computation of Internal and External Flows*, Vol. 2, Computational Methods for Inviscid and Viscous Flows, Wiley, Chichester, England, U.K., 1990.

[5]Thompson, K. W., "Time Dependent Boundary Conditions for Hyperbolic Systems, II," *Journal of Computational Physics*, Vol. 89, Aug. 1990, pp. 439–461.

[6]Gustafsson, B., "Far-Field Boundary Conditions for Time-Dependent Hyperbolic Systems," *SIAM Journal on Scientific and Statistic Computing*, Vol. 9, No. 5, 1988, pp. 812–828.

[7]Giles, M. B., "Non-Reflecting Boundary Conditions for Euler Equation Calculations," AIAA Paper 89-1942, June 1989.

[8]Kröner, D., "Absorbing Boundary Conditions for the Linearized Euler Equations," *Mathematics of Computation*, Vol. 57, No. 195, 1991, pp. 153–167.

[9]Sofronov, I. L., "Conditions for Complete Transparency on the Sphere for the Three-Dimensional Wave Equation," *Doklady Rossijskoy Akademii Nauk. Matematika*, Vol. 46, No. 2, 1993, pp. 397–401.

[10]Sofronov, I. L., "Artificial Boundary Conditions of Absolute Transparency for Two- and Three-Dimensional External Time-Dependent Scattering Problems," *European Journal of Applied Mathematics*, Vol. 9, No. 6, 1998, pp. 561–588.

[11]Sofronov, I. L., "Non-Reflecting Inflow and Outflow in a Wind Tunnel for Transonic Time-Accurate Simulation," *Journal of Mathematical Analysis and Applications*, Vol. 221, No. 1, 1998, pp. 92–115.

[12]Ballmann, J., and Sofronov, I., "Inviscid Flow Simulation in Channels with Time-Accurate Inlet and Outlet Conditions," *Proceedings of the 8th International Symposium on CFD*, ZARM Univ., Bremen, Germany, 1999, p. 1117; electronic version at http://www.zarm.uni-bremen.de/iscfd/.

[13]Hagstrom, T., Radiation Boundary Conditions for the Numerical Simulation of Waves, *Acta Numerica*, edited by A. Iserles, Vol. 8, Cambridge Univ. Press, Cambridge, England, U.K., 1999, pp. 47–106.

[14]Heinrich, R., Pahlke, K., and Bleecke, H., "A Three Dimensional Dual-Time Stepping Method for the Solution of the Unsteady Navier–Stokes Equations," *Proceedings of "Unsteady Aerodynamics" Conference*, London, 1996, pp. 5.1–5.12.

[15]Ferm, L., and Gustafsson, B., "A Downstream Boundary Procedure for the Euler Equations," *Computers and Fluids*, Vol. 10, No. 3, 1982, pp. 261–276.

[16]Kroll, N., Radespiel, R., and Rossow, C.-C., "The MEGAFLOW Project," *Aerospace Science and Technology*, Vol. 4, No. 4, 2000, pp. 223–237.

[17]Britten, G., and Ballmann, J., "Numerical Experiments about the Uniqueness of Aeroelastic Solutions of Elastic Wings in Transonic Flow," *NNFM72*, 1999, pp. 77–84.

[18]Radespiel, R., Rossow, C.-C., and Swanson, R. C., "Efficient Cell-Vertex Multigrid Scheme for the Three-Dimensional Navier–Stokes Equations," *AIAA Journal*, Vol. 28, No. 8, 1989, pp. 1464–1472.

[19]Jameson, A. J., "Time Dependent Calculation Using Multigrid, with Applications to Unsteady Flows Past Airfoils and Wings," AIAA Paper 91-1596, 1991.

[20]Ballmann, J., "Strömungsbeeinflussung und Strömungs-Struktur-Wechselwirkung an Tragflügeln. Erste Ergebnisse des SFB401 der RWTH Aachen," Deutsche Gesellschaft für Luft- und Raumfahrt, DGLR-JT99-189, Berlin, 1999.

[21]Moir, I. R. M., "Measurements on a Two-Dimensional Aerofoil with High-Lift Devices," AR-303, AGARD, Vol. 2, 1994, Test Case Number A2-1-12.

[22]Whitfield, D. L., and Janus, J. M., "Three-Dimensional Unsteady Euler Equations Solution Using Flux Vector Splitting," AIAA Paper 84-1552, June 1984.

[23]Runyan, H., and Watkins, C., "Considerations on the Effect of Wind Tunnel Walls on Oscillating Air Flow," NACA Rept. 1150, 1953.

[24]Abramowitz, M., and Stegun, I. A. (eds.), *Handbook of Mathematical Functions with Formulas, Graphs, and Mathematical Tables*, 14, Wiley-Interscience, New York, 1972.

J. Kallinderis
Associate Editor